Journal of Materials Science & Technology 270 (2026) 163–173

Contents lists available at ScienceDirect

Journal of Materials Science & Technology

journal homepage: www.elsevier.com/locate/jmst

Research Article

On the solute segregation to grain boundaries in SA508 steel

Przemysław Klupś[a,1,*], Benjamin M. Jenkins[a], Paul Chekhonin[b], James O. Douglas[a,1], Megan Carter[a,2], Yuanbo T. Tang[a,3], Jonathan M. Hyde[c,a], Nick Riddle[d], Paul A.J. Bagot[a], Michael P. Moody[a,4]

[a] Department of Materials, University of Oxford, Parks Road, Oxford OX1 3PH, UK
[b] Helmholtz-Zentrum Dresden-Rossendorf, Institute of Resource Ecology, Bautzner Landstraße 400, Dresden 01328, Germany
[c] UK National Nuclear Laboratory, D5, Culham Campus, Abingdon OX14 3DB, UK
[d] Rolls-Royce Plc., PO BOX 2000, Raynesway, Derby DE21 7XX, UK

ARTICLE INFO

Article history:
Received 29 September 2025
Revised 21 January 2026
Accepted 21 January 2026
Available online 26 January 2026

Keywords:
Temper embrittlement
GB segregation
Atom probe tomography
Bainitic steel
Phosphorus

ABSTRACT

Solute segregation to grain boundaries (GBs) within a high-Ni alloy (SA508 Grade 4N) aged at 427 °C was studied to investigate the role of phosphorus in causing non-hardening embrittlement in these steels. Electron backscatter diffraction (EBSD) and transmission Kikuchi diffraction (TKD) were employed to identify and characterise grain boundaries prior to targeted atom probe tomography (APT) analysis. Boundaries were classified as prior–austenite grain boundaries (PAGBs) and packet/block (lath) boundaries, enabling segregation behaviour to be directly correlated with crystallographic misorientation and boundary type. Distinct segregation patterns were observed at PAGBs compared to other boundaries, with strong anti–correlation between P/C and Ni/Mn/Si at PAGB interfaces. In unaged PAGBs, non–equilibrium segregation driven by vacancy drag promoted Ni enrichment, whereas W–shaped Ni concentration profiles in aged PAGBs indicate P–driven reverse vacancy flow. In contrast, solute enrichment at lath boundaries was found to depend strongly on misorientation angle. These results highlight the critical importance of controlling the 5-DoF when assessing segregation–driven embrittlement mechanisms in bainitic/martensitic steels. They also emphasise the potential of grain boundary engineering as a design strategy for improving resistance to embrittlement in nuclear and other demanding applications.

© 2026 Published by Elsevier Ltd on behalf of The editorial office of Journal of Materials Science & Technology. This is an open access article under the CC BY license (http://creativecommons.org/licenses/by/4.0/)

1. Introduction

An understanding of the degradation mechanisms can enable an improved prediction of the reactor pressure vessel (RPV) structural integrity through life. Margins in the safety case can then be reduced, enabling the reactor to operate longer safely via plant lifetime extension. To prolong the lifespan of a nuclear power plant, it is crucial to fully understand the embrittlement mechanisms that are currently viewed as limiting the safe operational lifetime of the RPV. The embrittlement can be defined as (1) a decrease in upper-shelf energy or (2) an increase in the temperature at which the material becomes brittle, also called Ductile-Brittle Transition Temperature (DBTT) [1]. If the increase in DBTT is sufficient, it could result in brittle failure of the RPV at the operating temperature or during cool-down in a reactor shutdown. This change in properties can be observed via Charpy impact testing [2].

Contributions to the overall embrittlement can broadly be grouped into two categories: hardening and non-hardening. In the first case, the embrittlement is correlated with increasing hardness of the material, i.e. the increase in DBTT correlates with the increase in hardness of the material. Whereas in the case of non-hardening, the embrittlement is linked to the weakening of grain boundaries (GBs) [3]. Hardening in the western-type reactor designs has been shown to be the dominant embrittling mechanism [4], and consequently, non-hardening embrittlement has not been studied in such detail. Regulatory approval for extension requires an accurate prediction of property changes, and while the contribution of non-hardening embrittlement to the overall embrittlement in the PWRs (Pressurised Water Reactors) is less common

* Corresponding author.
E-mail address: p.klups@imperial.ac.uk (P. Klupś).
[1] Present address: Department of Materials, Imperial College London, London SW7 2AZ, UK.
[2] Present address: Amentum, Thomson Ave, Harwell Campus, Didcot OX11 0GD, UK.
[3] Present address: School of Metallurgy and Materials, University of Birmingham, Birmingham B15 2TT, UK.
[4] Present address: ANSTO, New Illawarra Rd, Lucas Heights NSW 2234, Australia.

https://doi.org/10.1016/j.jmst.2026.01.027
1005-0302/© 2026 Published by Elsevier Ltd on behalf of The editorial office of Journal of Materials Science & Technology. This is an open access article under the CC BY license (http://creativecommons.org/licenses/by/4.0/)

[5], the risk must be minimised due to the potentially severe consequences. Hence, it is critical that we continue to study and to better understand GB embrittlement in RPV materials and the extent of its impact on mechanical properties.

Temper embrittlement (TE) is a significant cause of non-hardening embrittlement, occurring in martensitic/bainitic steels due to prolonged exposure to temperatures ranging from 400 to 600 °C [6]. It is widely acknowledged that the segregation of impurities and alloying elements at GBs plays a crucial role in TE [6,7]. This segregation can affect the cohesion of GBs through various chemical interactions, which can either strengthen or weaken the boundaries, depending on the elements present. In RPV steels, the solute that has been shown to affect mechanical properties most negatively within GBs is phosphorus (P) [8,9]. However, the effect of P atoms alone on TE remains unclear. Previous theoretical studies have concluded that the effect of P on the GB cohesion is not significant [10]. Instead, it was suggested that it is the P-X pairs which weaken the GBs.

Interestingly, until Ethan and Grabke [11], the effects of TE had been commonly observed in engineering alloy steels, but not in model Fe-P materials [12]. This led to the exploration of the effect of other alloy elements and the role of P-X pairs at the GBs. Subsequently, P has been observed to both segregate to GBs alone and also to co-segregate with other elements, including C, Cr, Mn, Mo, and Ni [11,13–18]. The relationship between bulk Ni composition and the measured P content in GBs has been widely investigated [19–22]. Kuleshova et al. [23] and Ševc et al. [24] found that P segregation increased with bulk Ni content in the alloy. Such co-segregation is enabled by thermal ageing of the material. Notably, the same study identified a negative correlation between the Ni and C found in bulk, which suggested P and C competition for sites within the GBs, as predicted previously by Park et al. [25]. P vs C competition has, however, been disputed due to the difference in size for each element, and their respective substitutional and interstitial nature [26].

The behaviour of transition metals (TMs)—Ni, Mn, and Mo—and their interactions with P gained significant interest as their bulk content coincided with TE [12]. Guttmann's theory of co-segregation associated TE with the synergistic co-segregation of P-TM pairs to GBs, where embrittlement-reducing TM solutes attract P and prevent it from segregation to the boundaries [27,28]. This theory, while challenged [29], still awaits further verification as the crystallographic nature of the GBs needs to be controlled in the studies.

Furthermore, some studies have associated the observed embrittlement with the segregation of the TMs [10,30] while others attribute it to the segregation of the P-TM pair [31]. Recent research by Mai et al. [32,33] attempted to decipher the effect of these pairs on TE. Using DFT simulations, they concluded that the segregation of P is unlikely to cause intergranular fracture via weakened interfacial bonding by itself. They surmised that the P atoms have relatively more repulsive interactions within the GBs as compared to TMs. Because increased levels of P segregation can cause the depletion of the previously segregated TM atoms, which have a positive effect on the GB cohesion, this will ultimately lead to TE. Moreover, the formation of some of the P-TM pairs, such as P-Mn or P-Cu, which are predicted to be cohesion-lowering, was found to be energetically favoured.

It is important to recognise that prior heat treatments that occur as part of the vessel manufacturing processes affect the distribution of P in the microstructure even before the material is exposed to irradiation. It has been previously observed that the amount of P at GBs is already at higher levels than in the matrix of the alloy before irradiation [34], which underlines the importance of investigating the controlled (unaged, non-irradiated) material.

Once the physical parameters of a GB are considered, the situation becomes more complex. The GB structure has been found to affect the P cosegregation [32]. Although the extent of segregation is correlated with misorientation angles of GBs [23,32], correlative measurements of both their compositional and structural nature, respectively, are, with some exceptions [35,36], not commonly reported. Nonetheless, one prominent study by Herbig et al. [37] has presented a relationship between C in GBs and their crystallographic misorientation relationships in nanocrystalline steel. The misorientation angles were measured using nanobeam diffraction in the scanning transmission electron microscopy (STEM). Subsequently, the same volumes of the material were characterised with atom probe tomography (APT) to measure the C content at the GBs, with the extent of the segregation quantified using the Gibbsian Interfacial Excess (Γ) method. The results implied a linear trend between the crystallographic misorientation low-angle GBs (LAGBs) and the Γ of C in those boundaries. However, in the case of high-angle GBs (HAGBs), there was no observable correlation. In the case of the former, it was demonstrated that the increased density of dislocations is partially responsible for the greater Γ values. Nonetheless, given the recent advances in the methodology [38], a more systematic and thorough approach to the relationship between GB misorientation and solute segregation has the potential to provide further important insights.

In this work, a high-Ni bainitic low-alloy steel was investigated, motivated by an observed change in its macro-scale mechanical properties after a relatively short exposure of up to 9 months to accelerated ageing at 427 °C (700 K). To investigate the origins of observed changes in non-hardening embrittlement, correlative, electron backscatter diffraction (EBSD), transmission Kikuchi diffraction (TKD) and APT were used to provide simultaneous structural and compositional characterisation of the GBs within the as-received material, and samples aged for 3 weeks and 9 months, respectively. The 3-week-aged samples were selected for further examination due to demonstrating the greatest single DBTT shift within the shortest ageing period.

2. Experimental

The nominal composition range of the investigated high-Ni steel is presented in Table 1. The material is classified as SA508 Grade 4N according to the ASME standard [39]. After being austenitised, the sample was cooled to room temperature at a rate allowing it to form a bainitic microstructure. Then, the sample was tempered at 650 °C and stress-relieved at 600 °C for 4 and 6 h, respectively.

The specimens were then exposed to long-term thermal ageing at a temperature significantly higher than those they would typically experience in a PWR, 427 °C (700 K) for 0.75, 1.5, 3, and 9 months, respectively. The aim was to increase the kinetics of microstructural change so they can be observed in a shorter experimental timeframe. This temperature was also selected in an attempt to ensure that the sample was restricted to the same thermodynamic regime as experienced in the reactor, as well as reaching similar levels of P segregation as during the PWR operational lifetime (see Fig. 1(b)). After each ageing period, several samples were taken out of the furnace, and Charpy impact tests were conducted at temperatures varying between −200 and 200 °C.

The Charpy impact testing was performed to ASTM E23 using standard V-notched specimens (10 mm × 10 mm × 55 mm). The other mechanical testing technique used in this study on all the samples is Vickers Hardness. Imaging for fractography of the fractured surfaces generated by the Charpy test was undertaken using optical microscopy.

The objective of conducting EBSD scans using the Nordlys Max EBSD system was to identify particular types of GBs such that APT analysis could target specific microstructure within the

Table 1
Nominal atomic and weight composition of the alloy tested, as well as ranges of weight compositions [40] for the SA508 4N type steel.

	Si	Ni	Mn	P	Cr	Mo	C	Cu
Sample (at.%)	0.19	3.41	0.29	0.008	1.81	0.29	0.87	0.025
Sample (wt.%)	0.10	3.84	0.31	0.005	1.81	0.53	0.20	0.03
SA508 4N (wt.%)	0–0.30	2.80–3.90	0.20–0.40	0–0.020	1.25–2.00	0.40–0.60	0–0.23	–

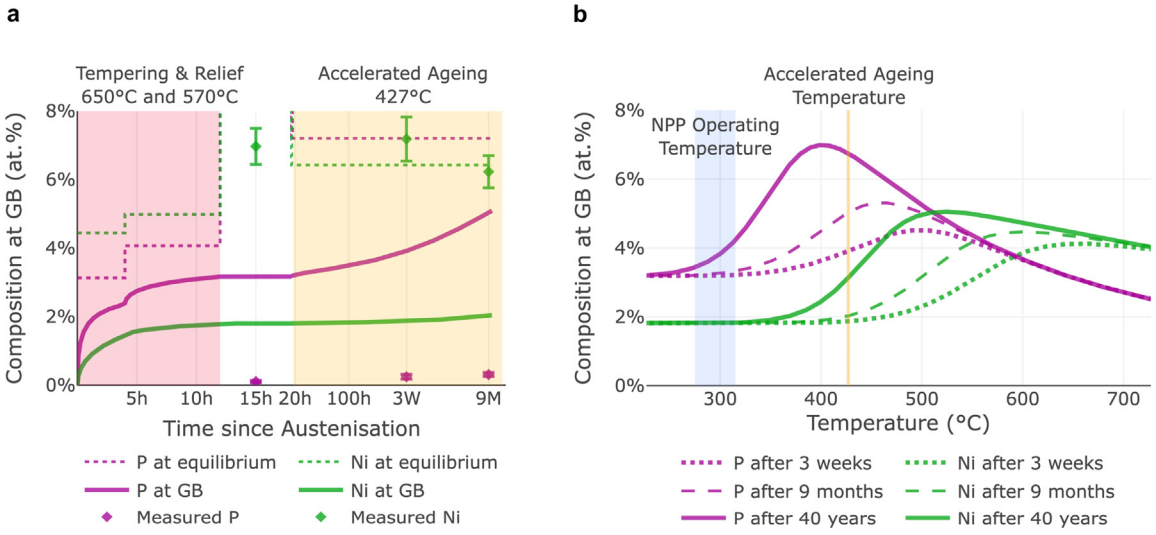


Fig. 1. (a) Predicted GB coverage during materials processing and accelerated ageing for Ni and P (solid green and magenta lines), their thermodynamic equilibria (dotted lines; off the scale at room temperature) at different temperatures. The collection of measured P and Ni concentrations is explained in the Experimental and Results sections. (b) Predicted concentration of Ni and P at the grain boundary in Fe-Ni and Fe-P systems if aged for 3 weeks, 9 months, and 40 years at given temperatures, respectively. Initial GB concentration was assumed to be 3.169 % for P and 1.800 % for Ni as seen at the 15 h mark in subplot (a).

accelerated ageing sample. For each EBSD scan, a large area of approx 100 µm × 200 µm was selected. The voltage was set to 15 kV and the probe current to 5 nA. To have a reasonable angular resolution, a prolonged exposure time exceeding 50 ms for each spot and a pixel size of 100 nm was used. Once the detector was calibrated and just before the start of the scan, a period between 1 and 3 h was observed for the stage to stabilise to minimise any thermal or beam drift during the scan. Each scan lasted for approximately 10 to 14 h.

To optimise the interpretation of the information obtained during the scan, and to improve the certainty that the targeted GB is correctly classified, an advanced EBSD evaluation was conducted. The analysis revealed that the bainitic transformation in this steel aligns closely with the Kurdjumov-Sachs (KS) orientation relationship. Consequently, packet, block, and lath boundaries[1] can have only specific misorientation angles and axes, which makes it possible to distinguish them from PAGB.[2] In the present steel, lath boundaries are limited to orientation angle intervals of [0° to 19°] and [51° to 60°].

Subsequent sample preparation for correlative TKD and APT was undertaken via Zeiss Crossbeam 550 with Zeiss Capella FIB and Gemini II SEM columns-Focused Ion Beam (FIB) instrument, where a beam of high-energy Ga^+ ions was used to conduct the site-specific lift-out process [24] with a desired feature (GB). Each sample was then attached to a silicon micropost [41] and milled further with a smaller current and higher precision, ultimately resulting in a 200-nm-thick lamella for TKD. Each specimen was subsequently milled into a needle-shape for APT, with the diameter at the apex not exceeding 120 nm.

TKD was used to characterise the 5 degrees of freedom (5-DoF) of the GBs [42] needed to define the crystallographic orientation of the respective grains in the remaining sample. GBs were assumed to be perpendicular to the *X* and *Y* axes of the TKD scans, which is a reasonable assumption based on the average grain size compared to the size of an APT sample.

During this project, the FIB sample preparation had to be performed with extreme care. Due to the 2D nature of the GBs, their increased chance of fracture during the experiment, and the relatively small volume of the sample which can be analysed in APT, the success rate of this procedure to encapsulate and image a GB did not exceed 30 %.

Once the GB had been targeted and shaped into a sufficiently small (< 120 nm) needle-shaped specimen, it was analysed in CAMECA LEAP 5000 XR using voltage-pulsing mode. For low-alloy steels, similar to those investigated in this study, the optimal parameters for high-quality APT data whilst maintaining acceptable yields of analysed volume have been investigated by Hyde et al. [43]. Based on these findings, these parameters were used for the experiments: 25 % pulse fraction, 0.30 % detection rate, 50 K specimen temperature, and 200 kHz pulse frequency.

The APT reconstructions were spatially calibrated using the limited crystallographic information retained by the analysis [44]. The presence of GBs in the APT data was usually indicated by a local change in composition due to solute segregation. Once a GB was detected, a Region of Interest (ROI) was defined, encapsulating part of this feature, in the form of a cuboid with one of its axes at the normal to the GB plane. The data from this ROI was exported, and a 1D concentration profile of the changing composition across the GB was generated. This data was subsequently analysed via GB Analysis Tool [45] to quantify solute segregation and deconvolute peak overlaps. This includes $^{58}Ni_2^+$ and $^{58}Fe_2^+$ peaks at 29 Da, which were deconvoluted using the known natural isotopic abun-

[1] to all three we will refer to as lath boundaries
[2] methodology explained in Appendix

dances of Ni from other peaks and assigning any excess of ions at the 29 Da peak to Fe.

3. Simulation

In this study, a GB structure was simplified to a perfect plane between two differently oriented crystals. The current understanding of these 2D features is that they are very complex and, in special cases, they can be described using a few parameters [46,47,7]. There are, however, some studies that attempt to understand and simulate segregation based on the distribution of solute energies [48]. Nonetheless, further research in this area is needed before the modelled output can realistically predict specific experimental results [49].

Simulating the thermodynamics and kinetics in a multi-solute and multiphase alloy can be challenging. To facilitate the task, it was assumed in the model that the material contained the nominal amounts of P and Ni and balanced Fe. The commonly used McLean-Langmuir model was applied. As the processing step, such as tempering, and the first weeks of ageing are assumed to have a critical importance on the GB segregation, the kinetics of this reaction must be included. Using further derivations of the McLean isotherm [50], we estimated how much solute is present in the GBs after a certain time. The cooling and heating steps were assumed to be instantaneous. The McLean-Langmuir formula for GB coverage at time t is presented in Eq. (1).

$$X(t) = (X_\infty - X_0)\left[1 - \exp\left(\zeta\right)\mathrm{erfc}\left(\sqrt{\zeta}\right)\right] + X_0 \tag{1}$$

where,

$$\zeta = \frac{4D_s t}{\beta^2 \delta^2} \tag{2}$$

where, X_0, $X(t)$, and X_∞ are the initial GB concentration, concentration after time t, and thermodynamic equilibrium of the boundary, respectively; β is the solute enrichment factor taken from Raabe et al. [51] (10^2 for Ni and 10^3 for P; both are assumed to be constant for all temperatures which is a simplification); δ is the GB thickness, constant for all calculations and assumed to be 0.5 nm; D_s is the diffusivity of the solute in BCC-Fe [52].

A section of the tempered and stress-relieved material was cut off and taken for the tests, while the remainder was placed into the furnace for accelerated ageing at 427 °C (700 K). A diagram showing both thermodynamic equilibria for both elements at each temperature, as well as estimated concentration for a better understanding of the effect of the kinetics, is shown in Fig. 1(a). Due to the simplicity of the model, the type of GB presented is not considered.

Although the thermodynamic equilibrium at higher temperatures during tempering and stress relief favours Ni segregation over P, the lower diffusivity of Ni does not enable it to reach its equilibrium in the given time period (12 h). As a result, between the processing stage and the ageing stage, the GB is expected to have more P than Ni.

Using the same model, Fig. 1(b) was created, whereby GB coverage of Ni and P is shown relative to the temperature. In the operating temperatures of the NPP, embrittlement due to P segregation is also expected, but at a significantly lower rate, as its concentration at the GB will only reach the levels of the 3-week sample from the experiment after 40 years of operation. This illustrates the appropriateness of this temperature range for the accelerated ageing study.

To reiterate, the McLean-Langmuir model has many drawbacks, and its usefulness in predicting segregation in engineering alloys should be treated with caution.[3] Nonetheless, its assumptions and limitations can be leveraged to explain discrepancies between predicted and experimental values. One of its limitations is the neglect of interactions between solutes. Therefore, the correlations between different solute segregation levels will be investigated in the latter part of this work. Another issue is that this model does not distinguish between different GB types or misorientation angles. Consequently, the segregation of certain solutes will be examined while controlling for GB type. Lastly, the model does not account for kinetic barriers, such as laths, that may prevent solutes from reaching their equilibrium levels. This, in effect, implies that the model may overestimate the segregation levels of solutes that face such barriers. This will be particularly relevant when comparing experimental to simulation results.

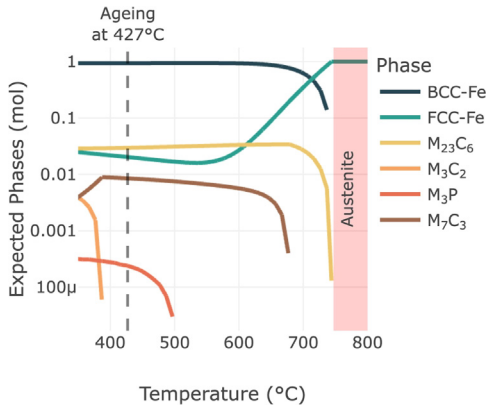


Fig. 2. Expected phases in the sample at different temperatures at their equilibrium as calculated with ThermoCalc Software.

Phase constituents in the material were calculated using the CALPHAD method (CALculation of PHAse Diagrams), implemented by the ThermoCalc software with the TCFE8.1 database. The mole fraction of the expected phases at equilibrium is presented as a function of temperature in Fig. 2.

It shows the mole fraction of expected phases at different temperatures at equilibrium, i.e. the kinetics were not considered. The carbides are expected to start forming only below the austenite temperature. Some of these carbides do contain Mo, which is also known to have a desired effect of limiting subsequent embrittlement as it scavenges P atoms in the matrix, preventing them from segregating to and weakening GBs [53]. Considering that some time is needed for the carbides to form and use up available Mo atoms, this coincides with P becoming free to roam around the material and reaching the boundaries only after the carbide formation has started. Additionally, the potential lack of M_3C_2 carbide at 427 °C is the drawback of this study, as its presence could alter the chemical potential of other solutes. Due to the low volume fraction expected, we will ignore its effect in this work.

4. Results

DBTT measurements are presented in Fig. 3(a) and Appendix B in the Supporting Information. While the upper shelf energy (US) was observed to decrease with ageing time, we concluded this trend to be an artefact of the measurement. The shift in the DBTT, which reliably increased with ageing time, indicates a genuine and independent embrittlement effect. Interestingly, half of the total DBTT shift achieved after 9 months (90 out of

[3] One of the issues is its sensitivity to some parameters. To address this, a Jupyter notebook file was provided in the Supplementary Material. It contains the Python script needed to replicate the simulation presented in this work.

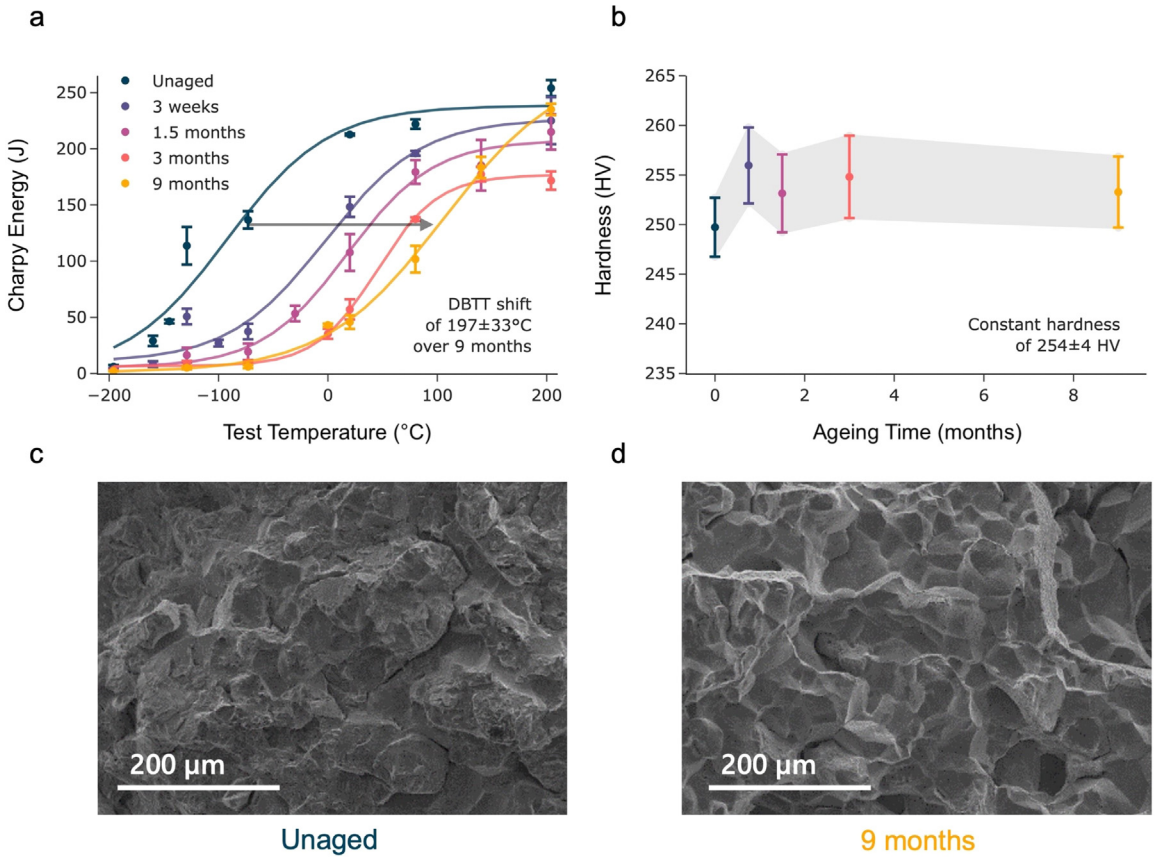


Fig. 3. (a) Charpy test showing DBTT shift, (b) stable Vickers hardness, (c) fractography of the unaged sample from the Charpy test at −196 °C, (d) fractography of the 9-month-aged sample from the Charpy test at 20 °C. Non-hardening embrittlement was further verified by intergranular fractures visible in the fractography images.

198 K) occurred within the first 3 weeks of thermal ageing, which suggests some critical behaviour occurs in the early stages of the thermal ageing at 427 °C. This rapid initial change is consistent with diffusion kinetics. Hypothesising that if grains are of similar size and spherical shape, and P atoms are equally distributed in each grain, most of these atoms will be closer to GB than to the centre of the grain. As diffusion distance is proportional to $\sqrt{t}$, the first half of all segregating P atoms will reach the GB significantly faster than the second half.

Vickers hardness was also measured. The results can be seen in Fig. 3(b) and show similar hardness values for all ageing times. The hardness can be considered constant within error, around 254 ± 4 HV. Values for all samples are available in Appendix B (see Table B.1).

The last characterisation of the macro-scale mechanical properties was fractography of the failed specimens from the Charpy tests, shown in Fig. 3(c and d). All fractography images contain some level of intergranular fractures, and the facets are the size of the known PAGB, which indicates that intergranular fracture occurs in all samples, including the unaged sample. Combining the results from all three tests above, it can be concluded that non-hardening embrittlement is the main phenomenon driving the shift in DBTT.

An example of a GB identified and characterised in the sequence of EBSD, TKD and APT described above is presented in Fig. 4. Three of the six PAGBs analysed are presented in Fig. 5. The localised maximal concentration of P has increased with each ageing time, but some P segregation was already present in the unaged sample. Further Γ values measured for all GBs detected are presented in Tables 2 and 3, while their averaged values can be found in Table 4, and visualised in Fig. 6, which shows a clear increase in Γ for Ni, Mn and P in lath boundaries. The main difference is in PAGBs, where for Ni and Mn, Γ is decreasing, while for P, Γ is increasing with ageing time.

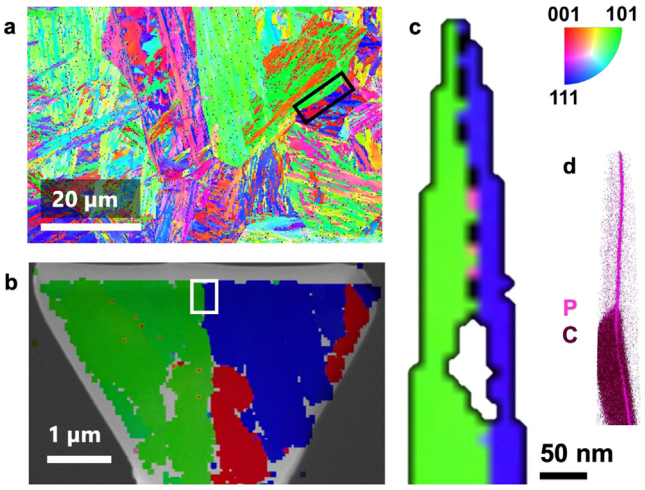


Fig. 4. An example of the typical analysis sequence for a selected GB (PAGB after 9 months of ageing): (a) EBSD scan shows the region from which the FIB lift-out was taken (black rectangle); (b) first and (c) second (subsequent to annular milling) TKD scans show further verification and accurate targeting of the GB; white rectangle in (b) shows the area from (c) before the second milling; (d) APT dataset shows a parallel GB with visible P segregation and a carbide at the bottom. Both (c) and (d) are shown at a similar scale. For visual clarity, only P and C atoms are shown. The stepped contour in (c) is caused by the limited resolution of the TKD.

The complexity of performing the experiments is a limiting factor for the number of Γ data points that can ultimately be col-

Table 2
Gibbsian interfacial excess (Γ) values and their corresponding errors in number of atoms/nm^2, derived by GB Analysis Tool [45], identified by reconstruction, ageing, GB type, misorientation angle (θ) and GB angle to the detector (α).

Reconstruction	Ageing	GB Type	θ (°)	α (°)	P	P error	Ni	Ni error	Mn	Mn error	Si	Si error	C	C error	Mo	Mo error
R5107_41273	Unaged	PAGB	24	49	0.38	0.03	5.09	0.21	1.18	0.08	0.74	0.08	−0.18	0.13	0.38	0.08
R5083_11488	Unaged	PAGB	34	73	−0.23	0.05	14.83	0.65	1.69	0.04	0.70	0.01	−1.57	0.24	0.53	0.04
R5083_11015	Unaged	Lath	7	133	−0.25	0.04	2.90	0.04	0.61	0.06	0.14	0.03	−0.53	0.09	−0.11	0.02
R5083_11860	Unaged	Lath	8	0	−0.09	0.01	−0.58	0.19	0.18	0.01	0.15	0.00	−0.12	0.01	−0.06	0.01
R5083_12018	Unaged	Lath	15	100	−0.01	0.04	4.05	0.59	−1.59	0.40	−1.42	0.39	−6.62	1.25	−4.63	0.98
R5107_41278	Unaged	Lath	55	78	0.14	0.03	5.19	0.08	0.97	0.03	0.38	0.00	0.14	0.27	1.26	0.08
R5083_11021	Unaged	Lath	59	95	0.23	0.01	5.25	0.31	0.79	0.01	0.05	0.15	0.91	0.12	0.51	0.08
R5083_08257	Unaged	Lath	60	71	−0.04	0.01	6.58	0.65	0.96	0.09	0.13	0.01	0.07	0.04	0.27	0.02
R5083_10880	Unaged	Lath	60	17	−0.06	0.00	3.12	0.15	0.68	0.02	0.00	0.02	−0.44	0.06	−0.07	0.03
R5107_51535	3 weeks	PAGB	43	73	0.63	0.02	1.73	0.76	1.34	0.01	0.03	0.08	2.65	0.30	2.81	0.08
R5107_31057	3 weeks	PAGB	57	34	0.16	0.05	4.71	0.00	1.16	0.03	0.60	0.02	1.16	0.06	3.38	0.05
R5107_31058	3 weeks	Lath	51	51	0.68	0.01	10.13	0.05	1.17	0.11	0.86	0.01	0.89	0.11	0.83	0.06
R5107_31034	3 weeks	Lath	56	57	0.39	0.06	6.88	0.09	1.51	0.02	0.62	0.07	0.81	0.37	3.23	0.20
R5107_51505	3 weeks	Lath	59	89	−0.00	0.01	6.38	0.25	0.86	0.01	0.15	0.01	0.46	0.01	0.68	0.01
R5107_31044	3 weeks	Lath	60	74	−0.00	0.01	4.27	0.21	0.92	0.10	0.21	0.03	−0.41	0.13	0.40	0.02
R5107_10627_a	9 months	PAGB	36	93	1.30	0.00	−0.47	0.28	0.68	0.07	0.10	0.04	1.62	0.06	2.15	0.03
R5107_10627_b	9 months	PAGB	36	93	0.95	0.01	1.45	0.19	0.75	0.02	0.60	0.02	0.77	0.01	1.12	0.01
R5107_10627_d	9 months	PAGB	36	93	1.08	0.01	7.12	0.40	1.49	0.02	0.70	0.01	1.75	0.08	1.40	0.02
R5107_10627_c	9 months	PAGB	36	93	1.17	0.01	0.40	0.32	0.70	0.04	0.20	0.02	1.42	0.03	1.63	0.03
R5107_10626	9 months	PAGB	49	113	0.56	0.04	1.45	0.61	0.94	0.02	0.05	0.24	0.62	0.02	1.51	0.03
R5083_10562	9 months	Lath	12	108	0.16	0.01	4.64	1.35	0.26	0.22	0.07	0.10	0.65	0.07	0.66	0.28
R5083_10740	9 months	Lath	55	162	0.38	0.03	8.36	0.25	0.70	0.13	0.39	0.03	1.06	0.07	1.64	0.02
R5083_07586	9 months	Lath	57	62	0.28	0.11	7.04	0.15	0.99	0.19	0.24	0.00	0.36	0.01	0.81	0.22
R5083_07595	9 months	Lath	59	110	1.05	0.01	15.62	2.52	3.41	0.32	1.06	0.07	4.50	0.84	3.43	0.26

Table 3
Continuation of Table 2. Crystallographic data derived from the TKD scans.

Reconstruction	Ageing	GB Type	θ (°)	α (°)	Rotation axis 1	Rotation axis 2	Rotation axis 3	v'a 1	v'a 2	v'a 3	v'b 1	v'b 2	v'b 3
R5107_41273	Unaged	PAGB	24	49	0.91	−0.26	−0.33	−5	12	−2	5	−9	−6
R5083_11488	Unaged	PAGB	34	73	−0.87	−0.26	−0.42	5	−9	7	12	6	−5
R5083_11015	Unaged	Lath	7	133	−0.65	0.75	−0.12	−8	0	1	12	1	2
R5083_11860	Unaged	Lath	8	0	−0.68	−0.49	0.54	10	11	7	−7	−6	5
R5083_12018	Unaged	Lath	15	100	−0.87	0.08	0.48	−12	−8	−1	9	7	2
R5107_41278	Unaged	Lath	55	78	−0.15	0.30	−0.94	5	−11	5	0	−12	−7
R5083_11021	Unaged	Lath	59	95	−0.14	−0.84	0.53	−10	−1	4	−3	−2	0
R5083_08257	Unaged	Lath	60	71	−0.17	0.34	−0.92	−9	3	−7	10	6	−1
R5083_10880	Unaged	Lath	60	17	0.05	0.99	−0.14	11	5	7	9	5	−9
R5107_51535	3 weeks	PAGB	43	73	−0.91	−0.39	−0.14	−12	−1	−12	1	−12	−1
R5107_31057	3 weeks	PAGB	57	34	−0.17	0.97	−0.15	−2	9	2	−11	−5	4
R5107_31058	3 weeks	Lath	51	51	−0.22	0.65	0.73	1	−4	1	10	−10	−7
R5107_31034	3 weeks	Lath	56	57	−0.04	−0.94	−0.33	1	10	1	6	−6	−5
R5107_51505	3 weeks	Lath	59	89	−0.08	−0.16	−0.98	1	−6	5	9	10	−1
R5107_31044	3 weeks	Lath	60	74	−0.89	0.29	0.34	3	4	1	11	11	−2
R5107_10627_a	9 months	PAGB	36	93	−0.28	−0.64	−0.71	−11	12	9	7	−2	6
R5107_10627_b	9 months	PAGB	36	93	−0.28	−0.64	−0.71	−11	12	9	7	−2	6
R5107_10627_d	9 months	PAGB	36	93	−0.28	−0.64	−0.71	−11	12	9	7	−2	6
R5107_10627_c	9 months	PAGB	36	93	−0.28	−0.64	−0.71	−11	12	9	7	−2	6
R5107_10626	9 months	PAGB	49	113	−0.93	0.08	0.37	10	−7	−2	3	−6	4
R5083_10562	9 months	Lath	12	108	−0.88	0.15	0.45	10	11	7	−5	10	−11
R5083_10740	9 months	Lath	55	162	−0.59	0.10	−0.80	7	11	6	6	4	−7
R5083_07586	9 months	Lath	57	62	−0.13	0.85	0.52	−1	6	−1	1	3	0
R5083_07595	9 months	Lath	59	110	−0.50	−0.41	−0.77	3	8	6	−5	−2	−1

Table 4
Average Γ values and their standard error for all boundaries grouped by different ageing times and GB types. Values for Mean and Standard Error of the Mean (SEM) are given in number of atoms/nm^2. Count represents the number of APT samples used for each group.

Ageing time	GB Type	P		Ni		Mn		Si		C		Cr		Mo		Count
		Mean	SEM	Mean	SEM	Mean	SEM	Mean	SEM	Mean	SEM	Mean	SEM	Mean	SEM	
Unaged	PAGB	0.07	0.31	9.96	4.87	1.43	0.25	0.72	0.02	−0.87	0.69	1.24	0.76	0.45	0.08	2
Unaged	Lath	−0.01	0.06	3.79	0.88	0.37	0.34	−0.08	0.23	−0.94	0.96	0.11	0.84	−0.4	0.73	7
3 weeks	PAGB	0.39	0.23	3.22	1.49	1.25	0.09	0.31	0.29	1.91	0.74	1.48	0.25	3.09	0.29	2
3 weeks	Lath	0.27	0.17	6.92	1.21	1.11	0.15	0.46	0.17	0.44	0.3	0.63	0.49	1.28	0.65	4
9 months	PAGB	1.01	0.13	1.99	1.33	0.91	0.15	0.33	0.13	1.24	0.23	0.08	0.25	1.56	0.17	2 (5)
9 months	Lath	0.47	0.2	8.92	2.36	1.34	0.71	0.44	0.22	1.64	0.96	0.29	0.33	1.63	0.64	4

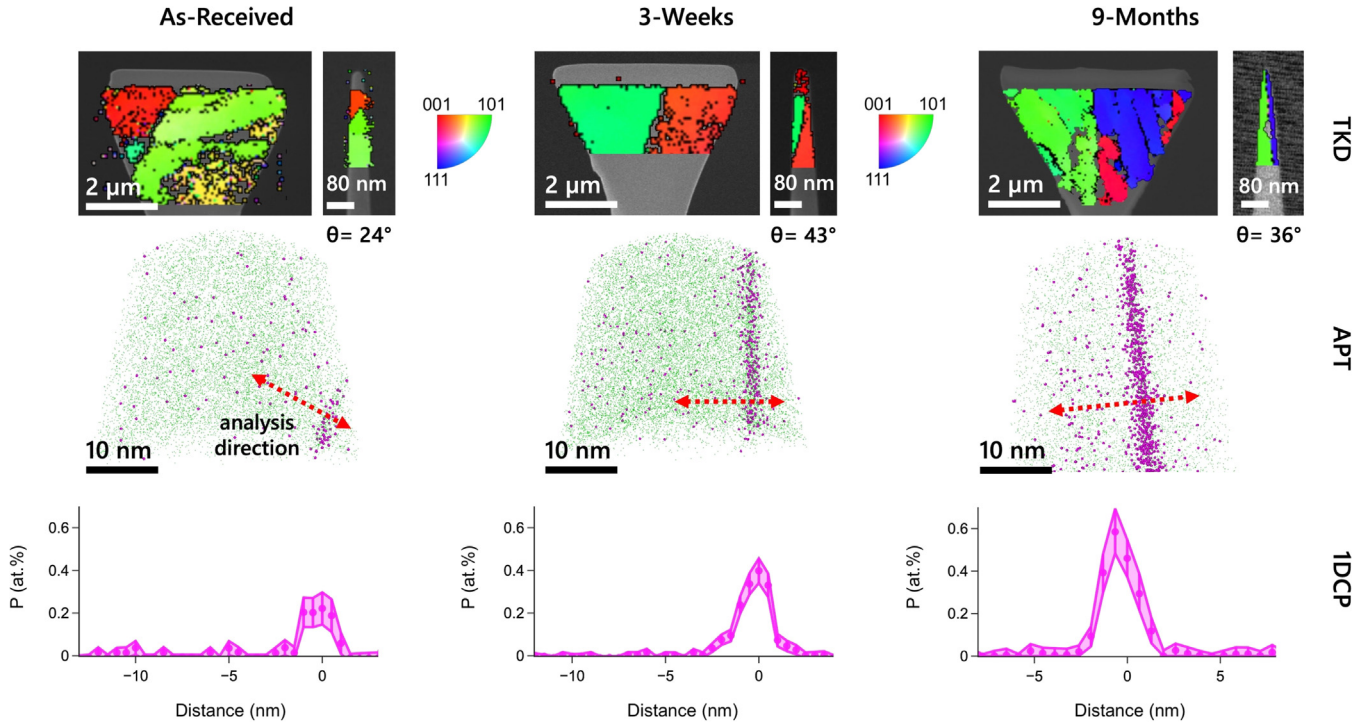


Fig. 5. Increasing P GB coverage with time in PAGBs. Top: TKD analysis of the sample during FIB preparation, pre- and post- annular milling. Middle: resulting reconstruction featuring GB with P (pink dots) segregation among Ni atoms (green dots). Bottom 1D concentration profile across the GB in the APT reconstruction.

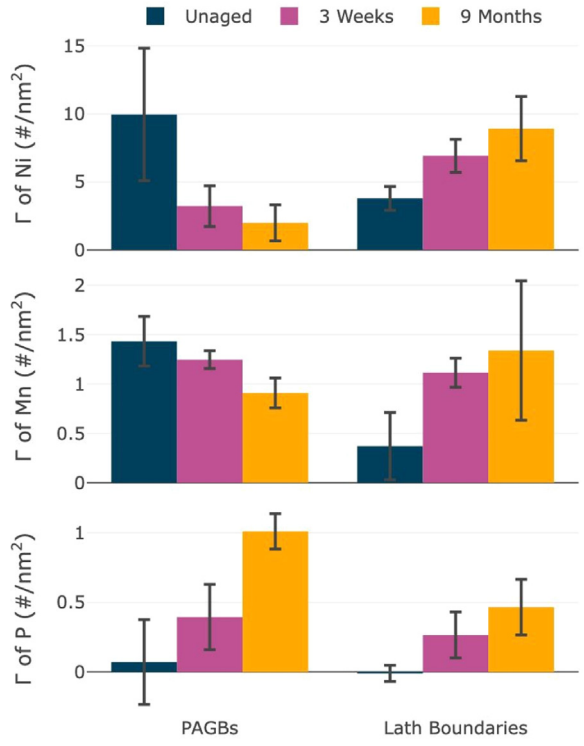


Fig. 6. Trends in Γ of Ni, Mn, and P in both GB types. The error bars show the standard error of the composition. Γ values can be negative when the concentration of an element in the interface is lower than in the adjacent regions.

lected. Hence, in the subsequent analysis and interpretation, each data point needs to be viewed with the caveat that other variables are not accounted for in this representation, e.g. the data point in the bottom right corner of Fig. 7(a) was taken from a small boundary plane situated between two carbide planes to which most of the P might have segregated. Possible aberrations might have also occurred due to nearby carbides [54], specifically ones that reside within the GBs but would not have been detected if they were outside the field of view of the atom probe. Additionally, due to the substantial difference in evaporation fields between C and Fe, the observed C distribution should be interpreted with caution. No precipitates or clustering were found in the matrix or GBs.

5. Discussion

The modelled scenarios using the McLean isotherm predicted a non-zero level of both P and Ni at GBs in the unaged samples. The resulting APT analyses show that while the concentration of Ni in PAGBs exceeds the expected value from the model, the P content is significantly lower in the unaged and 3-week-aged samples than the model predicts. In the subsequent ageing, whilst the experimental results showed that the level of Ni slowly decreased with time below its thermodynamic equilibrium, albeit not significantly, P concentration increased, but not to the predicted level. The reasons for these discrepancies can be manifold, as the model does not account for kinetic limitations, differences in boundary structures, inter-solute mechanisms, or non-equilibrium segregation (NES) effects.

This overestimation of P concentration can be attributed to kinetic suppression, where the short time at temperature during cooling and the complex bainitic microstructure prevented solute atoms from fully diffusing to GBs to reach true equilibrium. This can be particularly relevant for lath boundaries that form during the quench, where solutes must overcome kinetic barriers to reach these newly formed interfaces. In contrast, PAGBs were present during the entire heat treatment and thus had more time to accumulate solutes. This is supported by the higher overall segregation levels observed in PAGBs compared to lath boundaries.

As laths and PAGBs possess different structural characteristics, it is expected that they will exhibit different segregation behaviours.

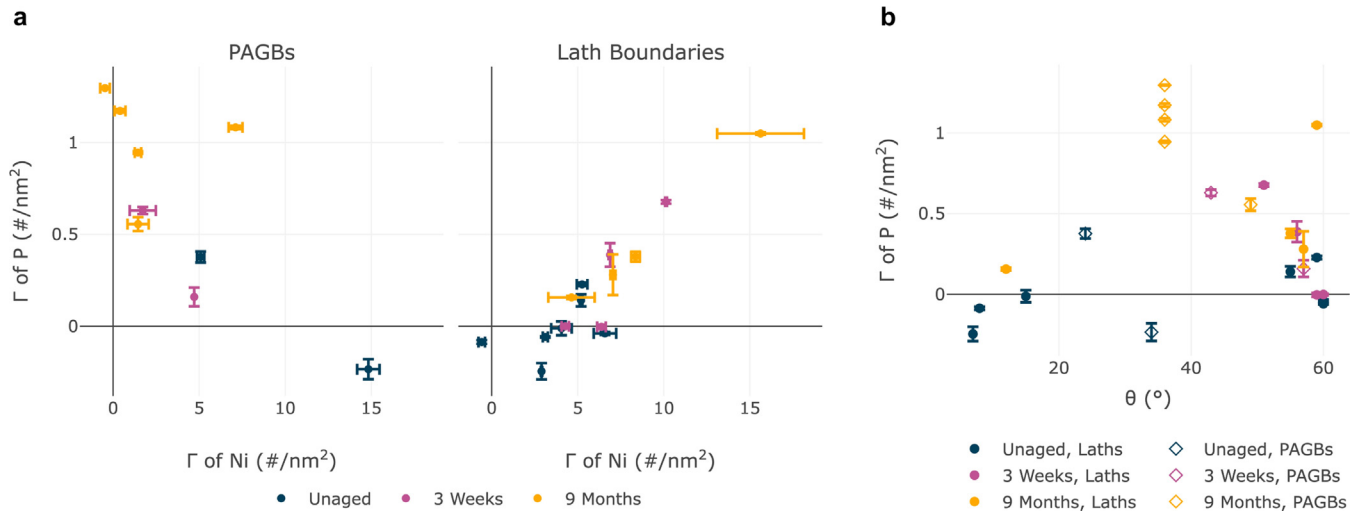


Fig. 7. (a) Relationship of Γ_P to Γ_{Ni} in PAGB and non-PAGB boundaries. (b) Γ_P and misorientation angle (θ) for all GBs found.

A simple comparison of Γ_P to misorientation angle (θ) was plotted in Fig. 7(b). At higher θ values majority of the data points follow a negative linear relationship, effectively decreasing solute concentration when θ approaches 60° Its effect suggests there might be some energetically preferred [55] crystallography at higher angles, which coincide with less additional space for solute. Additional linear regression analysis (presented in Appendix D) suggested that θ is a stronger predictor of the segregation than the ageing time in lath boundaries, whilst the opposite is true for PAGBs. This result resembles the correlations observed by Herbig et al. [37] but for higher θ, where deviation from the ideal angle provides higher dislocation density. Due to insufficient LAGBs found, this study could not replicate their findings on the linear relationship of Γ_C and θ. As the McLean model does not account for boundary structure or misorientation, these factors likely contribute to the discrepancies between model predictions and experimental observations.

To investigate the inter-solute relationships between the boundary segregation of solutes, Γ_P was plotted against the Γ_{Ni}, as presented in Fig. 7(a). This analysis has been further refined by grouping the data points into PAGBs and lath boundaries, respectively. The former shows an anticorrelation between these two elements, suggesting a possible competition for the same sites or a repulsion effect between these elements. With increasing ageing time, it is apparent that additional atoms of Ni are replaced with P, although not on a 1-to-1 basis. It should be emphasised that the complexity of the experiments and the relatively small number of data points acquired in this study limit the statistical confidence; therefore, all available data were included in the analysis.

To explore similar behaviour of other elements, we also investigated correlations between θ, ageing time, and Γ of selected elements: P, C, Mo, Ni, Mn, and Si for both PAGBs and lath boundaries.

Additionally, further linear regression experiments were conducted to examine the statistical significance of these results (see Appendix C). To summarise these findings, Fig. 8 presents two heatmaps with Pearson's correlation coefficients, corresponding to PAGBs and lath boundaries. Values closer to 1 or –1 signify correlation and anti-correlation, respectively, whereas values close to 0 indicate the lack of any correlation. The values should not be directly compared across the two subplots due to the different number of datapoints in each analysis.

In the case of the lath boundaries, no anti-correlations are observed between separate elements. This may suggest that these boundaries are not fully saturated and, thus, there is not yet significant site competition between these solutes. This is supported by (1) the total solute concentration being lower in PAGBs than in lath boundaries, and (2) all elements positively correlating with ageing time in lath boundaries, in contrast to PAGBs, where only P has a strong (> 0.5) positive correlation. This further supports the notion of P being the main contributor to this sample embrittlement.

On the other hand, upon examining the PAGBs in Fig. 8(a), the effect of θ on solute segregation is significantly less clear. Contrary to the case of lath boundaries, there are two separate groups of elements which anti-correlate with each other. However, these elements correlate with other elements inside the same group: when P and C increase in PAGBs, Ni, Mn and Si tend to decrease. In contrast to the lath boundaries, which do not show significant antagonisms or attractions between different elements, this suggests that PAGBs are, at least relatively, saturated.

The above findings are in agreement with previous studies: strong Ni-C antagonisms as well as Si-P were already published by Guttmann [56], who also reported a correlation between increased Mn and Ni levels and embrittlement. Although Ni and C do not occupy the same sites (substitutional and interstitial, respectively), there is a strong repulsion between them. Hence, if the boundary is saturated, anti-correlation of these elements is anticipated. The cosegregation of Mn, Ni, and Si elements is also expected. Apart from similar vacancy-binding properties [57], the occurrence of Mn-Ni-Si-rich clusters is well-documented in high-Ni low-alloy steels, and such steels favour their segregation, or even formation of thermodynamically stable phases, at heterogeneous sites [58].

The correlations apparent in Fig. 8 can also shed some light on the P-TM pairs and their effect on TE. As per Mai et al. [33], the competition has been observed only between P, Mn, and Ni if the bulk composition of TM is greater than 2.5 at.%, which is true for Ni in this sample. The same study concluded that the addition of P to Ni-rich GB can cause both site competition and repulsive interactions, causing Ni to leave the GBs and replacing it with P. This lowers the overall strength of the GB, contributing to its embrittlement. This finding is in agreement with our data under the condition that P-TM is interpreted as interactions between these elements present during the thermal ageing, not literal pairs bonded together.

Mai et al. [33] also predicted that Mo, which was expected to be displaced from GBs by P-Ni pairs, should have a significant influence. However, in this study, the role of Mo is inconclusive. To confirm the effect of Mo on P segregation in our findings, more characterisation of the carbides is needed. This would allow us to address the broader questions around where each solute is moving

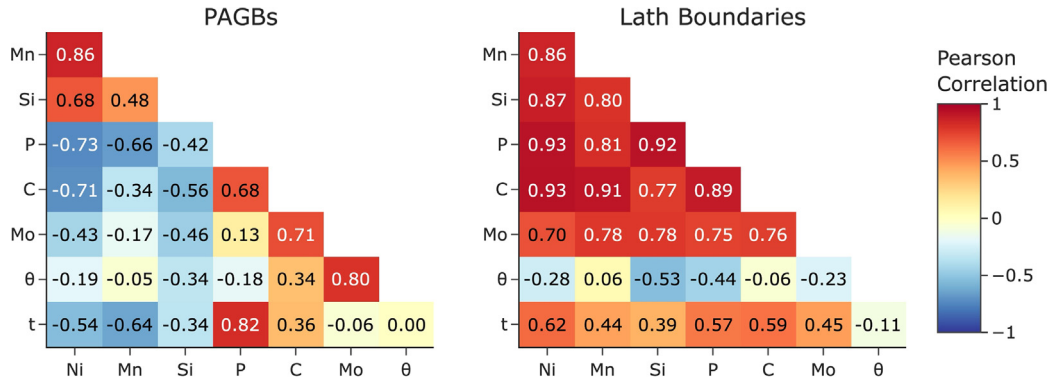


Fig. 8. Heatmaps with Pearson's correlation coefficients for misorientation angles (θ), ageing time (t), and Gibbsian interfacial excess (Γ) values for selected elements in PAGBs and lath boundaries.

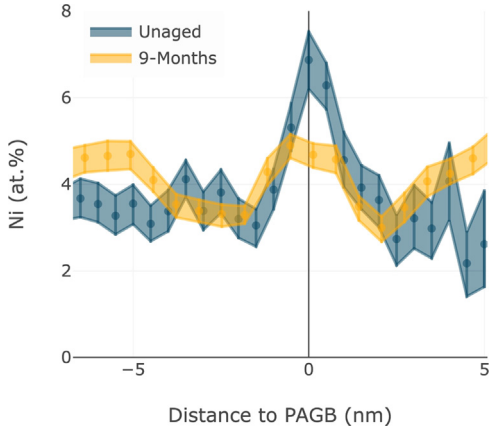


Fig. 9. Concentration profile of Ni in PAGB before and after 9 months of thermal ageing. After ageing, Ni shows a dampened peak at the GB, lower levels 3 nm away from the GB, followed by increased baseline Ni concentration 5 nm away from the GB. This characteristic W-shape may mean Ni is being depleted from the boundary and its near region, further into the adjacent regions. Error bars were derived from standard error values.

from/to. Unfortunately, the analysed volume of the APT data is not well suited for the size of these carbides, as they are too large and the data is not well representative of the entire microstructure. In future studies, it would be highly desirable to develop and use further complementary techniques, such as EPMA and STEM-EDS, that can further inform the nature of the microstructure in the vicinity from which the APT results are sampled.

Many of the boundaries investigated in this study were found to have a W-shaped profile, as shown in Fig. 9, that is characterised by augmentation and depletion regions around the GB. As a result, the integral of this composition yields a Γ value of zero or below, and thus this method of analysis is not recommended for GBs at non-equilibrium states [59], while other difficulties of the GIE metric have been already reported in literature [9]. Such a profile may well be an accurate representation of the Ni distribution.

Although one could consider it a potential APT artefact, we are confident it is a real distribution of Ni due to (1) observing these for multiple boundaries at different APT detection angles (α), and (2) similar observations found in irradiated steels [60,36]. Similar profiles have not been observed for other elements, most likely due to their significantly lower nominal compositions.

Considering that the increase in Ni gradient across the interface coincides with the depletion of Ni from PAGBs and its increase in PAGB-adjacent regions, it may be the case that we are observing a vacancy-driven reverse atom flow causing Ni depletion as described by Anthony [61]. If an attractive binding force between the vacancy and Ni is at the level of thermal energy, a solute is expected to move out of the vacancy sink towards the vacancy source. If, however, the binding energy between the solute and the vacancy is greater than the thermal energy in the system, solute enrichment by vacancy drag can be expected. In other words, the same movement of the vacancies during ageing may cause depletion of Ni (or other elements) as enrichment of elements with higher binding energy.

Not only can NES explain the W-profile, but also the initial oversaturation of Ni at PAGBs in the unaged condition. During rapid cooling, a substantial non-equilibrium vacancy flux rushes to the vacancy sinks such as PAGBs [61–63]. As the binding energy of Ni to vacancies exceeds the thermal energy, Ni atoms are efficiently dragged by the vacancy current, causing Ni to accumulate at the boundaries. Meanwhile, P atoms are being locked in by Mo before the carbides are fully formed [53]. Upon subsequent ageing at 427 °C, the system transitions into a new regime driven by the establishment of a vacancy depletion zone at the PAGBs. In this state, the local vacancy concentration gradient forces Ni due to its intermediate binding energy to undergo reverse atom flow. This causes the pre-existing Ni enrichment to decrease as Ni atoms diffuse out of the PAGB and into the adjacent regions, resulting in the depleted region of the observed W-profile. This outgoing Ni flux simultaneously clears the PAGB sites, allowing for the subsequent, and thermodynamically favoured, segregation of P, which follows a different diffusion mechanism (likely dumbbell diffusion [64]) and eventually replaces the transient Ni oversaturation.

Due to the possible vacancy transport of some solutes from GBs to adjacent regions, further investigation of trends in the composition of boundaries and adjacent regions in grains was conducted and shown in Fig. 10 and Table 5. This figure utilised the data from the GB Analysis Tool [45], i.e. concentration of the GB regions and the adjacent regions, which later enabled the derivation of Γ. Combining it with the grouping into GB types and ageing times, this figure provides a visualisation of where different solute elements may be diffusing and provides an alternative to Γ, which simplifies this information into one value. Additional tests exploring the statistical significance (available in Appendix E) further imply that while PAGBs show the signs of enrichment of the regions adjacent to GBs, the lath boundaries do not.

In Fig. 10, P increases in all GB types after ageing compared to the unaged sample, while its content in adjacent regions remains negligible, showing no clear trend. For PAGBs, bivariate regression analysis (see Appendix E) confirms that Ni, Mn, Si, and Mo in adjacent regions increase significantly with ageing. However, when comparing GB and adjacent-region compositions directly, elements such as Ni, Mn, and Si in PAGBs exhibit trends opposite to P, C,

Table 5
Mean concentrations in GBs and their adjacent regions, and their standard errors (SEM), measured from APT data in at.% units. The extent boundaries were detected using the GB Analysis Tool [45].

Ageing time	GB Type	Group	P		Ni		Mn		Si		C		Mo		Count
			Mean	SEM	Mean	SEM	Mean	SEM	Mean	SEM	Mean	SEM	Mean	SEM	
Unaged	PAGBs	Adjacent regions	0.02	0.01	4.05	0.17	0.23	0.02	0.18	0.02	0.17	0.05	0.19	0.02	4
Unaged	PAGBs	Boundary	0.22	0.14	8.42	1.96	1.05	0.31	0.48	0.09	0.26	0.08	0.51	0.13	2
Unaged	Lath boundaries	Adjacent regions	0.03	0.01	4.08	0.04	0.29	0.02	0.23	0.03	0.3	0.07	0.23	0.05	14
Unaged	Lath boundaries	Boundary	0.07	0.02	6.55	0.4	0.6	0.04	0.4	0.05	0.45	0.07	0.45	0.11	7
3 weeks	PAGBs	Adjacent regions	0.03	0.01	4.03	0.1	0.26	0.01	0.21	0.01	0.25	0.06	0.21	0.02	4
3 weeks	PAGBs	Boundary	0.32	0.07	7.06	0.58	1.05	0.23	0.48	0.09	1.06	0.42	1.87	0.64	2
3 weeks	Lath boundaries	Adjacent regions	0.03	0.01	3.99	0.11	0.28	0.02	0.21	0.01	0.17	0.04	0.22	0.02	8
3 weeks	Lath boundaries	Boundary	0.21	0.1	7.24	0.99	0.84	0.15	0.42	0.1	0.54	0.21	0.94	0.38	4
9 months	PAGBs	Adjacent regions	0.04	0.0	4.5	0.04	0.32	0.01	0.25	0.01	0.27	0.03	0.25	0.01	10 (4)
9 months	PAGBs	Boundary	0.43	0.05	5.64	0.26	0.74	0.05	0.44	0.03	0.68	0.09	0.85	0.05	5 (2)
9 months	Lath boundaries	Adjacent regions	0.03	0.0	4.14	0.11	0.33	0.02	0.23	0.01	0.25	0.05	0.21	0.03	8
9 months	Lath boundaries	Boundary	0.16	0.05	6.96	0.94	0.89	0.19	0.43	0.07	0.65	0.16	0.87	0.25	4

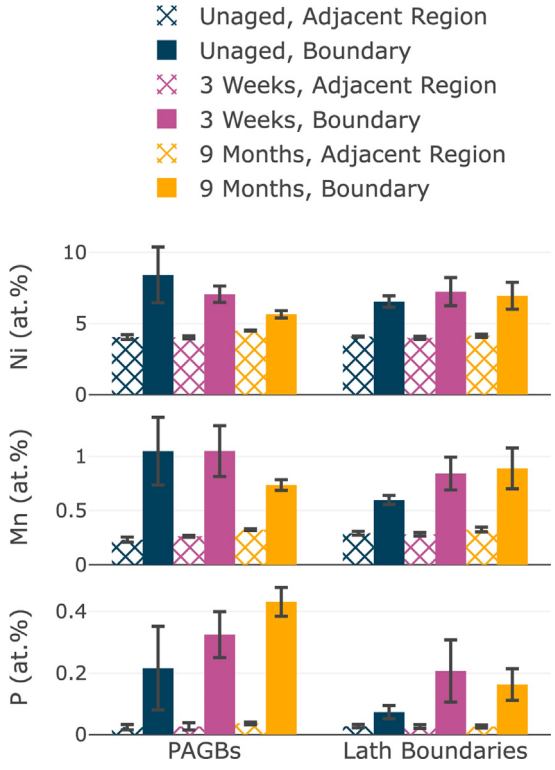


Fig. 10. Trends for concentration of selected elements in the boundary and adjacent regions grouped by GB types. Error bars show the standard error of the mean (SEM).

and Mo, supporting the NES and replacement hypotheses. This replacement likely drives small enrichments in adjacent regions for certain solutes during thermal ageing.

In contrast, lath boundaries show no statistically significant relationship between adjacent-region composition and ageing time. The coefficients for most of the elements in lath boundaries are positive in both difference and ratio analyses, implying that these boundaries are not saturated and may still be accumulating solutes, further supporting the kinetic barrier argument. Enlarged scatter in lath-boundary measurements, combined with the absence of consistent enrichment in adjacent regions, indicates a different segregation behaviour than in PAGBs.

6. Conclusions

In total, 21 GBs were analysed, 6 of which were PAGBs. Segregation of P and other solutes was quantified via Γ and compared across different ageing time and boundary types. A significant increase in P segregation over time was observed. Clear differences have been found between the segregation in PAGBs and other boundaries. Compared to the simulation results, there was significantly less P in the boundaries before the ageing started, while the levels of Ni, while initially oversaturated, started decreasing with ageing time. This difference has been attributed to the limitations of the McLean-Langmuir model, which failed to capture major processes as it does not control for GB type, kinetic barriers, NES, or inter-solute mechanisms.

By comparing the Γ levels for each solute to another, a strong anti-correlation of P and C to Ni, Mn, and Si has been observed in PAGBs. Further investigation showed W-profiles for Ni in such boundaries, implying that part of Ni residing in PAGBs was replaced by P and transported away from the boundary via vacancy flow, increasing its local concentration. This result is an experimental validation of some of the results from Mai et al. [32,33], e.g. P-Ni competition when Ni $>$ 2.5 at.%.

A negative relationship between the increasing misorientation angle and decreasing solute content was found in lath boundaries for many elements, such as P and Ni. This strong anti-correlation suggests a significant effect of GB structure on segregation levels in lath boundaries, potentially due to differences in the local dislocation density. It resembles the linear relationship of C segregation in LAGBs reported by Herbig et al. [37]. These relationships imply the necessity of controlling the 5-DoF of the boundary when estimating the segregation levels, especially if based on single measurements. They also emphasise the potential of grain boundary engineering to mitigate the embrittlement effects in the alloy design.

Further work incorporating techniques such as STEM-EDS or EPMA is needed to validate the distribution of Mo in the sample, specifically within carbides in order to establish whether the attraction between Mo and P, as proposed by the Guttmann theory of temper embrittlement [27,28], can account for the main cause of the non-hardening embrittlement.

Overall, this novel multi-technique characterisation study of the SA508-4 N steel has explored the interdependencies of solute segregation at the micro- as well as nanoscale. Investigating the behaviour of Ni and P in PAGBs can help with understanding not only the co-segregation of P-TM pairs but also of TE in general. Although such TE would not be expected in the PWRs when exposed to $<$ 300 °C, this study can facilitate a better understanding of the designs operating at higher temperatures. Further research can lead to more accurate predictions and increased longevity, safety, and economy of reactor pressure vessels in nuclear power plants, as well as any other critical components using such steels.

Data availability

The raw data required to reproduce these findings are available from the corresponding author on reasonable request.

Declaration of competing interest

The authors declare that they have no known competing financial interests or personal relationships that could have appeared to influence the work reported in this paper.

CRediT authorship contribution statement

Przemysław Klupś: Writing – original draft, Visualization, Software, Methodology, Investigation, Formal analysis, Data curation, Conceptualization. **Benjamin M. Jenkins:** Writing – review & editing, Validation, Supervision, Software, Methodology, Investigation, Conceptualization. **Paul Chekhonin:** Writing – review & editing, Validation, Software, Methodology, Investigation, Formal analysis. **James O. Douglas:** Writing – review & editing, Methodology, Investigation, Conceptualization. **Megan Carter:** Writing – review & editing, Investigation, Data curation. **Yuanbo T. Tang:** Writing – review & editing, Software, Investigation. **Jonathan M. Hyde:** Writing – review & editing, Supervision, Conceptualization. **Nick Riddle:** Writing – review & editing, Resources, Funding acquisition, Conceptualization. **Paul A.J. Bagot:** Supervision, Resources, Project administration, Methodology, Funding acquisition, Conceptualization. **Michael P. Moody:** Writing – review & editing, Supervision, Resources, Project administration, Methodology, Funding acquisition, Conceptualization.

Acknowledgements

We are thankful to Rolls-Royce Plc. for providing the necessary material for the case study. The atom probe facilities at the University of Oxford are funded by the EPSRC [grant number EP/M022803/1]. The authors acknowledge use of characterisation facilities within the David Cockayne Centre for Electron Microscopy, Department of Materials, University of Oxford, alongside financial support provided by the Henry Royce Institute [grant number EP/R010145/1]. P. Klupś would like to acknowledge the financial support of EPSRC and Rolls-Royce Plc. [grant numbers EP/R513295/1, 2113461].

Supplementary materials

Supplementary material associated with this article can be found, in the online version, at doi:10.1016/j.jmst.2026.01.027.

References

[1] G.R. Odette, P.M. Lombrozo, R. Wullaert, in: Effects of Radiation on Materials: Twelfth International Symposium, ASTM International, West Conshohocken, PA, 1984, pp. 840–860.
[2] M.K. Miller, M.N. Sokolov, R.K. Nanstad, K.F. Russell, J. Nucl. Mater. 351 (2006) 187–196.
[3] B. Bohanon, P. Wei, A. Foster, L. Bazar, Y. Zhang, D. Spearot, M. Bachhav, L. Capolungo, A. Aitkaliyeva, Prog. Nucl. Energy 174 (2024) 105276.
[4] M. Davies, A. Kryukov, C. English, Y. Nikolaev, W.L. Server, in: Effects of Radiation on Materials: 19th International Symposium, ASTM International, West Conshohocken, PA, 2000.
[5] J. Zelenty, Mater. Sci. Technol. 31 (2015) 981–988.
[6] C.L. Briant, S.K. Banerji, Int. Mater. Rev. 23 (1978) 164–199.
[7] P. Lejček, M. Šob, V. Paidar, Prog. Mater. Sci. 88 (2017) 83–139.
[8] R.A. Mulford, J.C. McMahon, D.P. Pope, H.C. Feng, Metall. Trans. A 7 (1976) 1183–1195.
[9] E.D. Hondros, M.P. Seah, S. Hofmann, P. Lejček, in: R.W. Cahn, P. Haasen (Eds.), Physical Metallurgy, Elsevier, Amsterdam, 1996, pp. 1201–1289.
[10] H.K.D.H. Bhadeshia, D.W. Suh, Ironmak. Steelmak. 42 (2015) 259–267.
[11] H. Erhart, H.J. Grabke, Met. Sci. 15 (1981) 401–408.
[12] V.V. Zabil'skii, Met. Sci. Heat Treat. 29 (1987) 32–42.
[13] S.G. Druce, G. Gage, G. Jordan, Acta Metall. Mater. 34 (1986) 641–652.
[14] S.G. Druce, Acta Metall. Mater. 34 (1986) 219–232.
[15] M.K. Miller, K.F. Russell, A. Jostsons, R.G. Blake, Appl. Surf. Sci. 87–88 (1995) 216–222.
[16] M.K. Miller, G.D.W. Smith, Appl. Surf. Sci. 87–88 (1995) 243–250.
[17] M.K. Miller, A. Cerezo, M. Hetherington, G.D.W. Smith, Atom Probe Field Ion Microscopy, Clarendon Press, Oxford, 1996.
[18] E. Meslin, B. Radiguet, P. Pareige, C. Toffolon, A. Barbu, Exp. Mech. 51 (2011) 1453–1458.
[19] R. Mulford, C. McMahon Jr, D. Pope, H. Feng, Metall. Trans. A 7 (1976) 1183–1195.
[20] C. Briant, Scr. Metall. 15 (1981) 1013–1018.
[21] M. Hashimoto, Y. Ishida, R. Yamamoto, M. Doyama, Acta Metall. Mater. 32 (1984) 1–11.
[22] H. Kimura, K. Abiko, S. Suzuki, MRS Online Proc. Libr. 122 (1988) 379.
[23] E.A. Kuleshova, B.A. Gurovich, Z.V. Lavrukhina, M.V. Saltykov, S.A. Fedotova, A.N. Khodan, J. Nucl. Mater. 479 (2016) 110–122.
[24] P. Ševc, J. Janovec, P. Lejček, P. Záhumensky, J. Blach, Scr. Mater. 46 (2002) 7–12.
[25] S.G. Park, K.H. Lee, K.D. Min, M.C. Kim, B.S. Lee, J. Nucl. Mater. 425 (2012) 1–8.
[26] P. Lejček, S. Hofmann, J. Phys.: Condens. Matter 28 (2016) 064001.
[27] M. Guttmann, Met. Sci. 10 (1976) 337–341.
[28] M. Guttmann, P. Dumoulin, M. Wayman, Metall. Trans. A 13 (1982) 1693–1711.
[29] H.J. Grabke, K. Hennesen, R. Möller, W. Wei, Scr. Metall. Mater. 21 (1987) 1329–1334.
[30] D. Raabe, B. Sun, A.K.D. Silva, B. Gault, H. Yen, K. Sedighiani, P.T. Sukumar, I.S. Filho, S. Katnagallu, E. Jägle, P. Kürnsteiner, Metall. Mater. Trans. A 51 (2020) 5517–5586.
[31] M. Nasim, B.C. Edwards, E.A. Wilson, Mater. Sci Eng. A 281 (2000) 56–67.
[32] H.L. Mai, X.Y. Cui, D. Scheiber, L. Romaner, S.P. Ringer, Acta Mater. 231 (2022) 117902.
[33] H.L. Mai, X.Y. Cui, D. Scheiber, L. Romaner, S.P. Ringer, Acta Mater. 250 (2023) 118850.
[34] B.A. Gurovich, E.A. Kuleshova, Y.I. Shtrombakh, O.O. Zabusov, E.A. Krasikov, J. Nucl. Mater. 279 (2000) 259–272.
[35] L. Zhang, B. Radiguet, P. Todeschini, C. Domain, Y. Shen, P. Pareige, J. Nucl. Mater. 514 (2019) 434–443.
[36] Q. Chen, H. Rong, J. Shenbao, X. Fei, S. Gang, Acta Mater. 220 (2021) 117297.
[37] M. Herbig, D. Raabe, Y.J. Li, P. Choi, S. Zaefferer, S. Goto, Phys. Rev. Lett. 112 (2014) 126103.
[38] K. Babinsky, R.D. Kloe, H. Clemens, S. Primig, Ultramicroscopy 136 (2014) 9–18.
[39] B.S. Lee, M.C. Kim, J.H. Yoon, J.H. Hong, Int. J. Pres. Ves. Pip. 87 (2010) 74–80.
[40] https://www.steeldata.info/std/demo/demo/data/9540.html, 06-07-2025.
[41] K. Thompson, D.B. Lawrence, D.J. Larson, J.D. Olson, T.F. Kelly, B. Gorman, Ultramicroscopy 107 (2007) 131–139.
[42] B.M. Jenkins, D.F.M. Gouné, P.A.J. Bagot, Z. Peng, M.P. Moody, B. Gault, Appl. Surf. Sci. 504 (2020) 147011.
[43] J.M. Hyde, E.A. Marquis, K.B. Wilford, T.J. Williams, Ultramicroscopy 111 (2011) 440–447.
[44] B. Gault, M.P. Moody, F.D. Geuser, G. Tsafnat, A.L. Fontaine, L.T. Stephenson, D. Haley, S.P. Ringer, J. Appl. Phys. 105 (2009) 104501.
[45] B. Jenkins, https://github.com/jenjamin/APT-Grain-Boundary-Analy, June, 2020.
[46] P. Lejček, S. Hofmann, Crit. Rev. Solid State 20 (1995) 1–85.
[47] P. Lejček, M. Šob, J. Mater. Sci. 49 (2014) 2477–2482.
[48] L. Huber, R. Hadian, B. Grabowski, J. Neugebauer, npj Comput. Mater. 4 (2018) 1–8.
[49] P. Lejček, M. Všianská, M. Šob, J. Mater. Res. 33 (2018) 2647–2660.
[50] B.S. Bokshtein, A.N. Khodan, O.O. Zabusov, D.V. Maltsev, B.A. Gurovich, Phys. Met. Metall. 115 (2014) 146–156.
[51] D. Raabe, M. Herbig, S. Sandlöbes, Y.J. Li, D. Tytko, M. Kuzmina, D. Ponge, P. Choi, Curr. Opin. Solid State Mater. Sci. 18 (2014) 253–261.
[52] W.F. Gale, T.C. Totemeier, Smithells Metals Reference Book, 8th Ed., Elsevier, Amsterdam, 2003.
[53] P. Dumoulin, M. Guttmann, M. Foucault, M. Palmier, M. Wayman, M. Biscondi, Met. Sci. 14 (1980) 1–15.
[54] W. Sha, L. Chang, G.D.W. Smith, L. Cheng, E.J. Mittemeijer, Surf. Sci. 266 (1992) 416–423.
[55] D.G. Brandon, Acta Metall. Mater. 14 (1966) 1479–1484.
[56] M. Guttmann, J. Phys. 5 (C7) (1995) 85–96.
[57] T. Whiting, D. King, M. Wenman, J. Nucl. Mater. 542 (2020) 152429.
[58] H. Ke, P. Wells, P.D. Edmondson, N. Almirall, L. Barnard, G.R. Odette, D. Morgan, Acta Mater. 138 (2017) 10–26.
[59] B.M. Jenkins, D.F.M. Gouné, P.A.J. Bagot, Z. Peng, M.P. Moody, B. Gault, Microsc. Microanal. 26 (2020) 247–257.
[60] C.M. Barr, P.J. Felfer, J.I. Cole, M.L. Taheri, J. Nucl. Mater. 509 (2018) 181–190.
[61] T.R. Anthony, Acta Metall. Mater. 17 (1969) 603–609.
[62] K. Aust, R. Hanneman, P. Niessen, J. Westbrook, Acta Metall. Mater. 16 (1968) 291–302.
[63] R. Faulkner, Acta Metall. Mater. 35 (1987) 2905–2914.
[64] L. Messina, T. Schuler, M. Nastar, M.C. Marinica, P. Olsson, Acta Mater. 183 (2020) 166–185.